IAEA
International Atomic Energy Agency

20th IAEA Fusion Energy Conference
Vilamoura, Portugal, 1 to 6 November 2004

IAEA-CN-116/TH/P3-9

RECENT ADVANCES IN THE THEORY AND SIMULATION OF PELLET ABLATION AND FAST FUEL RELOCATION IN TOKAMAKS

P.B. PARKS, L.R. BAYLOR,[1] R. ISHIZAKI,[2] S.C. JARDIN,[3] and R. SAMTANEY[3]

General Atomics
San Diego, California 92186-5608
United States of America

[1]Oak Ridge National Laboratory, Oak Ridge, Tennessee, USA
[2]National Institute for Fusion Science, Toki, Japan
[3]Princeton Plasma Physics Laboratory, Princeton, New Jersey, USA

Recent Advances in the Theory and Simulation of Pellet Ablation and Fast Fuel Relocation in Tokamaks

P.B. Parks,[1] L.R. Baylor,[2] R. Ishizaki,[3] S.C. Jardin,[4] and R. Samtaney[4]

[1]General Atomics, P.O. Box 85608, San Diego, California 92186-5608, USA
[2]Oak Ridge National Laboratory, Oak Ridge, Tennessee 37381, USA
[3]National Institute for Fusion Science, Toki, Japan
[4]Princeton Plasma Physics Laboratory, Princeton, New Jersey

email: parks@fusion.gat.com

Abstract. This paper presents new theory and simulation of pellet ablation, and the rapid cross-field redistribution of the ionized pellet mass following pellet injection in tokamaks. The first 2-D time-dependent simulations describing the expansion of pellet ablation flow against the magnetic field is presented here using the Eulerian code CAP. The early-time expansion is characterized by the formation of an ellipsoidal diamagnetic cavity surrounding the pellet, which diverts heat flux around the pellet, thereby reducing the ablation rate. Near-pellet cloud properties from CAP provide initial conditions for the subsequent E/B advection of the ionized clouds caused by polarization in the inhomogeneous toroidal magnetic field. The first complete set of time-dependent equations describing mass redistribution has been developed and solved for numerically using the PRL code. New effects identified, including curvature drive by near sonic field-aligned flows, rotational transform of the magnetic field lines and magnetic shear are considered from the viewpoint of the parallel vorticity equation. Close agreement between theory and experimental fuel deposition profiles are obtained for both inner and outer wall pellet injection on the DIII-D tokamak, providing improved predictive capability for ITER. A new 3-D MHD simulation code AMR was started, which provides the required fine-scale mesh size needed for accurate modeling of pellet clouds having sharp perpendicular-to-B gradients.

1. Introduction

High-density plasma operation, most readily produced by depositing fuel in the central regions of the tokamak by pellet injection, is crucial for meeting fusion power performance requirements in next step devices such as ITER. This paper presents new theory and simulations of pellet ablation, and the rapid cross-field redistribution of the ablated and ionized pellet substance following pellet injection in tokamaks. A new time-dependent Eulerian code CAP was developed to study pellet ablation in 2-D axisymmetric (r,z) geometry. Recently, CAP was used to study pellet deformations resulting from non-uniform illumination by the plasma electron heat flux streaming along the magnetic field lines to the pellet [1]. In those simulations the magnetic field was assumed to be straight and uniform, and its influence on the ionized ablation flow was not taken into account. Presented in Sec. 2 are the first pellet ablation simulations using the full set of time-dependent 2D resistive magnetohydrodynamic equations to study the interaction between the ablation flow and the magnetic field. In this approach the field-aligned and transverse expansion of the pellet cloud with respect to the magnetic field is finally treated self-consistently. When the heat flux to the pellet is instantly switched on, a high-pressure ionized ablation cloud forms near the pellet, which pushes away the magnetic field and forms a diamagnetic cavity with a $\beta \approx 1$ boundary. Since the cavity excludes magnetic flux near the pellet, the electron heat flux guided by the field lines to the pellet can be reduced by a great deal, thus prolonging the lifetime and penetration depth of the pellet.

In Sec. 3 we present two theoretical drift models. One is a semi-analytic model [2], which agrees well with the DIII-D experiments, and is then used to predict the fueling source profile in ITER. The other approach is a fully 3-D MHD simulation using the AMR code (Sec. 4). Results from AMR, though preliminary, have much in common with the analytical model and the experimental results.

2. Fully 2D Pellet Ablation Including Interaction With the Magnetic Field

The CAP code uses an Eulerian approach based on the cubic-interpolated pseudoparticle (CIP) method. The CIP numerical scheme has two important features. One is that it is designed to accurately resolve fine-scale temperature and density structure near the interface between two disparate regions, for example, a shock surface. The other is that it can treat the nebulous boundary layer where the solid undergoes transformation to a gas and the pellet surface recedes. In that sense, the CIP method is particularly suitable for the study of pellet ablation involving the interaction between a compressible phase (abated material) and an incompressible phase, (the cold pellet), and was recently used to explore pellet deformation due to asymmetric ablation pressures [1]. We have just started to include the 2D MHD effects, mainly the important the $J \times B$ force inhibiting the cross-field expansion of the of the resistive ablation flow. The MHD approach evolves the time-dependent magnetic field induction equation together with the flow conservation equations. We consider an idealized situation where the plasma heat flux falling on the pellet is switched on at $t = 0$ and is then constant — in actuality the heat flux varies during pellet entry. Preliminary simulation results are presented for a deuterium pellet with radius $r_p = 2$ mm, immersed in plasma with undisturbed parameters: $n_{e\infty 14} = 1$, $T_{e\infty} = 2$ keV, and $B_\infty = 1$ T. Subindex ∞ denotes a plasma equilibrium quantity. The external plasma is assumed to be a mass-less zero-pressure medium with infinite electrical conductivity $\sigma_\infty = \infty$. In Figs.1 and 2 is shown the temporal evolution of cloud parameters at 0.4 μs, the duration of the simulation. At that moment the ablation cloud is not yet fully developed; the initial expanding ablation layer formed around the pellet has a cross-field thickness of 5 pellet radii. Figure 1 shows respectively, contour plots of the density, and profiles along the r (midplane) and z (axis) of the pellet. At a distance of $\sim 5\, r_p$, the density of the expanding cloud has fallen to a density of $2.5 \times 10^{17}\,\mathrm{cm}^{-3}$ and yet still remains almost spherical, as the cloud pressure still exceeds the magnetic field pressure at that radius. Figure 2 shows ablation pressure profiles in the corresponding r and z directions. In Fig. 3 we plot magnetic pressure B^2, clearly indicating that a diamagnetic cavity has been formed around the pellet by the piston action of the high dynamic pressure of the ablation layer. The magnetic field, piles up at the edge of the cavity, which has a $\beta = 1$ boundary radius of $r_c \approx 6.5\, r_p$, and becomes strongly rarefied in the cross-section of the pellet pellet. On this time scale, the magnetic flux Φ trapped between the axis of the pellet and the moving boundary remains nearly constant in time and equal to the initial flux $\Phi(t=0) \approx \pi r_p^2 B_\infty$ threading the pellet. The benefit of the magnetic cavity is that the incident electron heat flux constrained to follow the lines of force will be partially diverted around the pellet, the flux being reduced by just $B/B_\infty < 1$. As a

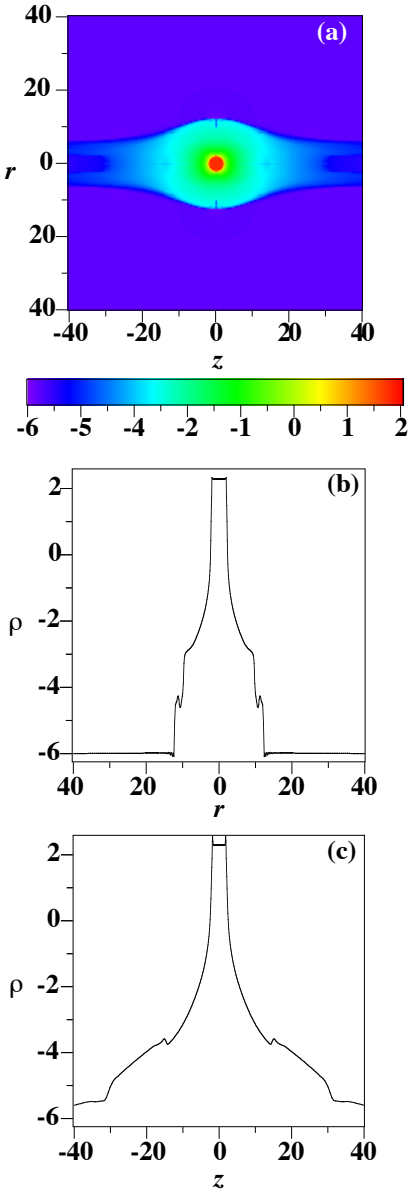

Fig. 1 (a) Mass density isosurfaces after 0.4 μs. (b) corresponding radial midplane profile ($z = 0$), and (c) axial profile ($r = 0$). The units are kg/m^3, and log10 scale is used.

result, the ablation rate and ablation pressure are reduced by $(B/B_\infty)^{1/3} \sim (r_p/r_c)^{2/3}$, and $(B/B_\infty)^{2/3} \sim (r_p/r_c)^{4/3}$, respectively. So far, our results do not yet include heat flux divergence, so that a fully self-consistent treatment of the ablation rate awaits further study.

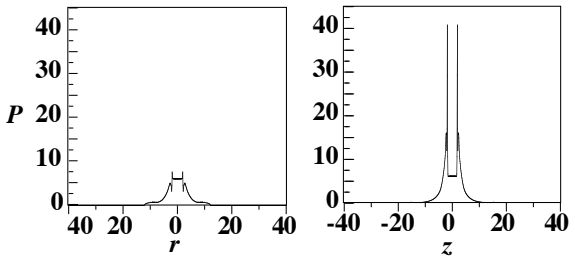

Fig. 2. Pressure profiles in the ablation cloud (a) readial midplane profile (z=0), and (c) axial profile (r=0). The units are MPa.

3. Semi-Analytical Drift Model Using Parallel Vorticity Equation

This section summarizes the current semi-analytic drift model [2] and provides a set of fully time-dependent ODEs describing the cross-field drift velocity of an ionized cloudlet $\vec{v}_{\perp c} = \{v_{\rho c}, v_{\chi c}\}$ with respect to the magnetic axis of a tokamak. A plane polar coordinate system for a near circular, high-aspect-ratio toroidal plasma is used: $\vec{\rho} = \{\rho,\chi\}$, where ρ is the radial (flux surface) label, χ the poloidal angle, $R = R_0 + \rho\cos\chi$, and R_0 is the major radius of the magnetic axis. The new properties of the described model involve: 1) enhanced curvature drive associated with near-sonic parallel flows; 2) incorporation of realistic (non flat) plasma pressure profiles; 3) helical magnetic field line geometry (rotational transform); and 4) "mass shedding" caused by the disabling effect of magnetic shear on the coherency of the E/B cloud drift. These new effects have not been addressed in previous theoretical models, which were of two basic variants: the "continuous sheet stream" model [3] and the "discrete cloudlet" model [4]. Although those models illuminated part of the drift physics, they were not sufficiently developed to allow meaningful comparison with actual experimental fuel deposition profiles. In this letter we build upon the latter approach. The supposition is that the pellet ablation process periodically forms a series of fully-ionized, cylindrical cloudlets aligned among B. From this point on, we assume that the initial parameters of the cloudlets: radius r_c, half-length L_c $(L_c >> r_c)$, density n_0, temperature T_0, and pressure $p_0 = 2n_0T_0$, can be determined by the scaling formulas derived in Ref. [4].

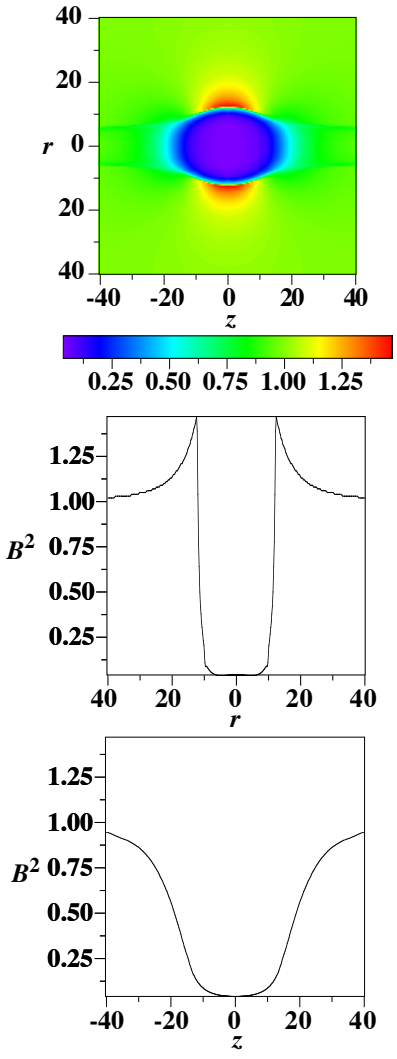

Fig. 3. (a) Contours of B^2 after 0.4 microsec. (b) corresponding radial mid-plane profile (z = 0), and (c) axial profile (r = 0). Here, B is normalized to 1.121 T.

The drifting and longitudinally expanding cloudlet (r_c remains fixed) represents a localized perturbation in pressure $\tilde{p} = p_c - p_\infty$, and flow velocity $\vec{v}$. Though the initial cloudlet pressure $p_c = p_0$ can be almost an order of magnitude larger than p_∞ [4], still, $\beta_c = 2\mu_0 p_c / B_\infty^2 << 1$ in the long expanding cloud filament. The two components of the transverse drift velocity require two equations. The first is the perturbed vorticityequation, which can be obtained from expanded quantities defined as $J_\parallel = J_{\parallel\infty} + J_\parallel$ and $B^2 \cong B_\infty^2 + 2\vec{B}_\infty \cdot \tilde{B}$ and then using transverse pressure balance $0 \cong \nabla_\perp(\tilde{p} + \vec{B}_\infty \cdot \tilde{B}/\mu_0) + O(\delta)$ where $\delta = r_c/R << 1$ to eliminate the magnetic perturbation, obtaining [2]

$$\frac{\hat{b}}{B}\cdot\nabla\times mn\frac{d\vec{v}}{dt}=(\vec{B}\cdot\nabla)\frac{\tilde{J}_{\|}}{B}-\frac{2(\hat{b}\times\vec{\kappa})\cdot\nabla_{\perp}\tilde{p}}{\mu_0 B} \quad . \tag{1}$$

Here $d/dt=\partial/\partial t+\vec{v}\cdot\nabla$, $\vec{\kappa}=\hat{b}\cdot\nabla\hat{b}$ is the curvature of the magnetic field lines, and m is the ion mass. The curvature of the field line is left unchanged by cloud perturbations to order δ. Since $\delta << 1$, the approximation $\nabla\cdot\vec{v}_{\perp}\cong 0$, provides the second equation.

In Eq. (1), we put $\vec{v}=v_{\|}\hat{b}+\vec{v}_{\perp}$, and $D/Dt=\partial/\partial t+\vec{v}_{\perp}\cdot\nabla_{\perp}$. After inserting the result into Eq. (1), we find that the centrifugal force term $v_{\|}^2\vec{\kappa}$ dominates all other terms containing $v_{\|}$ which are either smaller by order δ, or do not contribute in the end results [2]. We then obtain an equation for the evolution of the electrostatic potential,

$$\nabla_{\perp}\cdot\left(\frac{mn}{B^2}\frac{D\nabla_{\perp}\Phi}{Dt}\right)=(\vec{B}\cdot\nabla)\frac{\tilde{J}_{\|}}{B}+\frac{(\hat{b}\times\vec{\kappa})\cdot\nabla_{\perp}(2\tilde{p}+mnv_{\|}^2)}{B} \quad . \tag{2}$$

The important inference is that even when the cloud pressure comes to equilibrium by expansion, $\tilde{p}\cong 0$, the curvature drive stemming from the centrifugal force still persists, because the cloudlet continues expanding ($v_{\|}^2>0$) at nearly constant pressure, much like a heated balloon maintained at atmospheric pressure. It will be more convenient to evaluate the curvature drive term in the rest frame of the cloudlet. Thus we introduce the local magnetic field line following coordinate system $\{x,\ y,\ z\}$ or $\{r,\ \vartheta,\ z\}$, with $x=r\cos\vartheta$, $y=r\sin\vartheta$. Here x = const, y = const, labels a helical magnetic field line, and z is distance along a field line coinciding with the cloud centroid location ($x=0, y=0$). The orthogonal unit vectors $\hat{x}=\hat{\rho}$ and $\hat{y}$ point in the x and y directions, i.e., normal to a magnetic surface and binormal to the field line. In describing the localized cloudlet flows, the small angle $\sim B_{\chi}/B << 1$ between the $\vec{x}\equiv\{x,\ y\}$ and $\vec{\rho}$ (poloidal) planes is of relatively minor consequence. Any cloud quantity $A(r,z)$ is assumed to be axisymmetric $\partial A/\partial\vartheta=0$, and symmetric $A(r,z)=A(r,-z)$ about the cloud midplane location ($z=0$). Now let $\vec{\rho}_{c0}(t)=\{\rho_c(t),\chi_{c0}(t)\}$ be the instantaneous position of the cloud origin ($x=y=z=0$), and let $\vec{\rho}_c(t)=\{\rho_c(t),\chi_c(t,z)\}$ designate the coordinate of a point somewhere along the cloud centroid. Then $\chi_c(t,z)=\chi_{c0}(t)+z/q_c(t)R_0$, where $q_c(t)\equiv q[\rho_c(t)]$, is the safety factor in the cloud rest frame. From a vector addition $\vec{\rho}=\vec{\rho}_c(t)+\vec{x}$, one readily derives

$$x=\rho\cos[\chi-\chi_c(t,z)]-\rho_c(t),\quad y=\rho\sin[\chi-\chi_c(t,z)] \quad . \tag{3}$$

$$\hat{\rho}\cdot\hat{r}=\cos\vartheta\cos[\chi-\chi_c(z,t)]+\sin\vartheta\sin[\chi-\chi_c(z,t)] \quad . \tag{4a}$$

$$\hat{\chi}\cdot\hat{r}=\sin\vartheta\cos[\chi-\chi_c(z,t)]-\cos\vartheta\sin[\chi-\chi_c(z,t)] \quad . \tag{4b}$$

With the usual approximation in Eq. (2), $\vec{\kappa}\cong-\hat{R}/R$, we obtain exactly $\hat{b}\times\hat{\kappa}\cdot\nabla_{\perp}=-[\sin\vartheta\cos\chi_c(z,t)+\cos\vartheta\sin\chi_c(z,t)]/R\,(\partial/\partial r)$. We treat R as constant hereafter. Recalling that $\hat{b}\cdot\nabla\Phi=0$ near the cloud, Φ is independent of z, and can be solved for by integrating Eq. (2) along the length of the cloud, from $z=-L(t)$ to $L(t)$:

$$\nabla_{\perp}\cdot\vec{\Gamma}=\frac{-1}{BR}\left[\sin\vartheta\cos\chi_{c0}(t)+\cos\vartheta\sin\chi_{c0}(t)\right]$$

$$\int_0^{L(t)}\frac{\partial}{\partial r}(2\tilde{p}+mnv_{\|}^2)\cos[z/q_c(t)R_0]dz \quad . \tag{5}$$

The notation

$$\vec{\Gamma} = \frac{m\tau}{B^2}\left\{\frac{\partial \nabla_\perp \Phi}{\partial t} + (\vec{\mathrm{v}}_\perp \cdot \nabla_\perp)\nabla_\perp \Phi\right\} + \frac{\nabla_\perp \Phi}{\mu_0 c_{A\infty}} \quad ,$$

$$\tau(r,t) = \int_0^{L(t)} n(r,z,t)dz \quad , \tag{6}$$

refers to, respectively, the line-averaged inertial (ion polarization) drift current, and the column density. The last term in $\vec{\Gamma}$ represents the parallel return current carried by outgoing shear-Alfvén waves with velocity $c_{A\infty}$, i.e., $\tilde{J}_\parallel(z=L) = -\nabla_\perp^2 \Phi/(\mu_0 c_{A\infty})$ [4]. The presence of the $\cos(z/q_c R_0)$ factor in Eq. (6), stems from the rotational transform. As z increases the grad-B drift current rotates *relative to the* $\{x, y\}$ *coordinates* to which the electrostatic field and charge distribution are effectively frozen into. Toroidicity in this sense can thus become important if the expansion length $L(t)$ should become an appreciable fraction of the connection length $q\pi R_0/2$.

To find a closed form solution of Eq. (5) it may be assumed that all quantities inside the cloud are uniform in a transverse plane, obtaining

$$\nabla_\perp \cdot \vec{\Gamma} = \frac{2}{BR}\delta(r - r_c)\left[\sin\vartheta\cos\chi_{c0}(t) + \cos\vartheta\sin\chi_{c0}(t)\right]\Psi(t) \quad , \tag{7}$$

where the "toroidal drive" integral

$$\Psi(t) = \int_0^{L(t)} [p_c(t,z) - p_\infty(t) + M_c^2(z,t)]\cos[z/q(t)R]dz \quad , \tag{8}$$

includes the effect of real (non-uniform) plasma profiles, $p_\infty(t) \equiv p_\infty\left[\rho_c(t)\right]$, although n_∞ is considered uniform. The background pressure (temperature) profile can seriously limit cloud penetration depth for inboard pellet injection compared to previous model calculations [2,3] since the cloud is drifting from the plasma edge up the pressure gradient, reducing Ψ. To evaluate Ψ, the pressure and velocity evolution along B is obtained from the 1-D Lagrangian fluid code PRL, described in Refs. [2,4].

Thus, at any arbitrary instant, the electrostatic potential obeys Poisson's equation $\nabla_\perp^2 \Phi = 0$ in each region. After employing continuity of Φ at $r = r_c$, the potential in the tokamak frame (but expressed using cloud frame coordinates) reads

$$\Phi = \begin{cases} \Phi_{in} = C(t)y + [D(t) - E_{\rho\infty}(t)]x & r < r_c \\ \Phi_{out} = C(t)\dfrac{r_c^2}{r}\sin\vartheta + D(t)\dfrac{r_c^2}{r}\cos\vartheta - E_{\rho\infty}(t)x & r > r_c \end{cases} \tag{9}$$

The boundary condition at $r \to \infty$ was predicated on the assumption that the background tokamak radial electric field changes slowly on the scale of the cloud dimensions, so it can be written as $E_{\rho\infty}(t) \equiv E_{\rho\infty}[\rho_c(t)]$. The potential represents the superposition of two mutually orthogonal dipoles, with dipole constants C and D that are clearly related to the time-dependent cloud (or centroid origin) velocity components $C = -\mathrm{v}_{\rho c}B$, $D = \mathrm{v}_{\chi c0}B + E_{\rho\infty}(\rho_c)$, in which $\mathrm{v}_{\chi c0}(t) = \rho_c(t)\partial\chi_{c0}(t)/\partial t$ and $\mathrm{v}_{\rho c}(t) = \partial\rho_c(t)/\partial t$. To resolve the dipole constants, we apply the divergence theorem to Eq. (7). After a few steps we get two equations for C and D, which translates into two equations for the radial and poloidal cloud centroid drift velocities [2]. We use rescaled variables, $t = t/(L_c/c_0)$, and $\mathrm{v} = \mathrm{v}/c_0$, to write the equations in non-dimensional form

$$M(t)\frac{d\mathrm{v}_\rho}{dt} = -\nu_{drag}\mathrm{v}_\rho + g\tilde{\Psi}(t)\cos\chi_{c0}(t) + wM(t)\frac{\mathrm{v}_\chi \mathrm{v}'_\chi}{\tilde{\rho}_c} \quad , \tag{10a}$$

$$M(t)\frac{dv_\chi}{dt} = -\nu_{drag}[v_\chi - v_E(\tilde{\rho}_c)] - g\tilde{\Psi}(t)\sin\chi_{c0}(t) - wM(t)\frac{v_\rho v'_\chi}{\tilde{\rho}_c}, \quad (10b)$$

The other normalized quantities are defined as $\tilde{\rho}_c = \rho_c/a$, $w = L_c/a$, $\tilde{\Psi} = \Psi/p_0 L_c$, $g = 2L_c/\tilde{\tau}R$, $\tilde{\tau} = \tau_{in}(0)/n_0 L_c$ (~ 1), $M = \tau_{in}(t)/\tau_{in}(0)$, $d\tilde{\rho}_c/dt = wv_\rho$, and v_E is the normalized plasma $E_{\rho\infty} \times B$ convective velocity. The dimensionless damping coefficient associated with Alfvén wave emission is $\nu_{drag} = (2/\tilde{\tau})(n_\infty/n_0)(c_{A\infty}/c_0)$. New nonlinear velocity terms appearing in Eqs. (10) come from the polarization current generated by the centrifugal and Coriolis forces acting on a cloud brought into poloidal rotation either by spin-up or by simply launching the pellet off the midplane, making $\sin\chi_{c0}(t)$ in Eq. (10b) non-zero at $t = 0$. The primed notation connotes a subtle difference between the two forms of poloidal rotation velocity, $v'_\chi = (\rho_c/w)\partial\chi_c(z,t)/\partial t$, and $v_\chi = (\rho_c/w)\partial\chi_{c0}(t)/\partial t$. In the absence of magnetic shear, $dq/d\rho = 0$, we see that $v'_\chi = v_\chi$. With non-zero magnetic shear, it may be verified that a small difference arises $\delta v_\chi \equiv v'_\chi - v_\chi = v_\rho z/L_s$, where $L_s = qR_0/\hat{s}$ is the magnetic shear scale length and $\hat{s} = (\rho/q)(dq/d\rho)$ is the usual shear parameter. Physically, magnetic shear twists the flux tube/cloud cross-section, changing the circular cloud boundary into a rotated ellipse, which rotates and flattens with longitudinal distance z, without changing its cross-sectional area. Elliptical compression brings the charge layers closer together in the x-direction as z increases, which results in a differential drift of the cloud segments in the y-direction with respect to the center of the circular segments of the cloud near the cloud symmetry plane $z = 0$. Thus, beginning with the Lagrangian fluid cells at the ends of the cloud, the cells sequentially "peel off' one by one and get deposited in the plasma; the prescription for varying $M(t)$ and thus the mass depositionn rate is given in Ref. [2].

Modeling of the pellet mass redistribution and resulting deposition in the DIII-D tokamak has been undertaken by solving Eqs. (10) together with the parallel dynamics using PRL. A pellet ablation code is used to track the pellet/plasma parameters along the pellet trajectory. Then the location and parameters of the cloudlets produced by the pellet along its ablation track are obtained using Ref. [4] scaling laws. The resulting deposition profile for midplane outer wall $\chi_{c0}(0) = 0$, and above midplane inner wall $\chi_{c0}(0) \sim 3\pi/4$ pellet injection cases on DIII-D are shown in Fig. 4. The electron density perturbation measured by Thomson scattering less than 1 ms after the ablation process is overlaid. The present model compares well with measured profiles immediately following pellet injection in both cases. It should be mentioned that in the outer wall injection case, the theory and experimental profiles deviate sharply for $\rho/a > \sim 0.85$. This is likely due to a strong edge localized mode (ELM) triggered during the pellet injection event, which causes a large fraction of the edge pedestal density to be ejected from the plasma. This is also consistent with the modest discrepancy between the experimental and calculated particle fueling efficiencies, 46% vs 66%, respectively. For inner wall injection the triggered ELM is much less pronounced; both measured and calculated fueling efficiencies are ~100%.

Figure 5(a) shows how the deposition profiles vary with analytical q-profiles displayed in Fig. 5(b). Parameters of an ITER-scaled device are used: 6 mm deuterium pellet with velocity 300 m/s entering from inboard side at 45 deg below the midplane, $\chi_{c0}(0) = 5\pi/4$; central and pedestal temperatures are 20 keV and 4 keV, respectively. As expected, we see that a flatter q (weaker shear) throughout most of the plasma volume, promotes deeper fuel penetration by reducing the mass shedding, as explained above.

4. Progress on 3D Simulation Using Adaptive Mesh Refinement (AMR) Code

The AMR method is intended to provide an accurate and efficient simulation of the MHD processes responsible for redistribution of pellet clouds [5]. Ideal MHD conservation equations are solved with heuristic sources to simplify the computational scheme. In the continuity equation, a moving density source with strength equal to the local pellet ablation rate, has a spherically symmetric Gaussian distribution centered about the pellet, with a

characteristic size equal to 10 r_p. Particles released by the pellet are assumed to be *stationary* in the pellet reference frame (no initial expansion velocity). Heating dynamics are circumvented on subsequent cloud expansion time scale by assuming that each particle released by the source is instantaneously heated to the local plasma background temperature T. When the pellet passes across a flux surface, the plasma temperature on that surface changes in time by dilution cooling, i.e., the energy content within a toroidal flux shell is unchanged by the addition of particles ablated from the pellet, $n(t)T(t) = n_\infty T_\infty$. In actuality, the cloud temperature is much smaller, because the heating time of newly ablated particles is comparable to the expansion flow time scale. The initial plasma conditions and magnetic field are determined by solving the Grad-Shafranov equilibrium equation, in which p_∞ and T_∞. are flux functions and n_∞ is spatially uniform.

The AMR numerical method employs a finite volume technique wherein each variable is stored at the cell center. The numerical fluxes of conserved quantities are obtained at the cell faces using a combination of the 8-wave formulation [6] and unsplit upwinding [7,8]. Second order is achieved by fitting a linear profile within each cell with Van Leer type slope limiting to ensure monotonicity. The method is essentially a predictor-corrector type method in which we extrapolate the cell-centered values onto the faces in each finite volume at time step n+1/2. These are then used to compute the fluxes across the faces which are then used to obtain the cell-centered conserved quantities at the next time step.

We present preliminary results for a hydrogen pellet with a velocity of 3200 m/s and radius r_p = 1 mm entering a tokamak plasma with minor radius a = 0.26 m, magnetic field B_∞ = 0.23 T. Pellet entry from both inboard and outboard sides of the tokamak is considered, such that the initial location of the pellet is on the same flux surface. Figure 6 shows a density isosurface for inboard (midplane) injection, at times t = 2, 20, and 60 Alfvén times $a/c_{A\infty}$. The left part of the image at each time depicts the isosurface in the physical domain, while the right side shows the outlines of the various grids in the calculation where mesh adaptivitiy has taken place. At t = 2 the pellet ablated mass is roughly in the shape of an ellipsoid with its major axis aligned along the magnetic field lines. For t > 2, the dominant mass

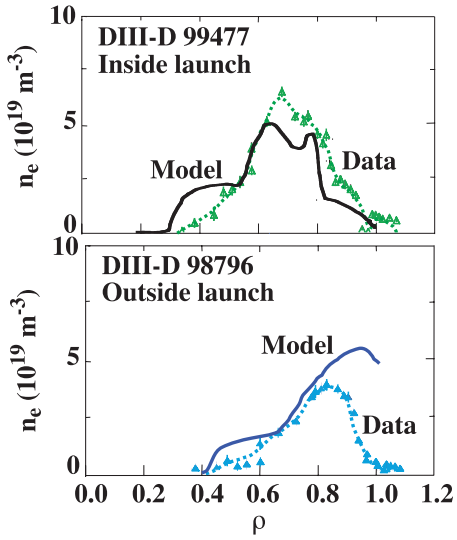

Fig. 4. (a) Measured pellet mass deposition from a 2.7 mm cylindrical D_2 pellet (equivalent spherical radius 1.54 mm) injected at 153 m/s from the inside wall 35 cm above the midplane, $\chi_{c0}(0) \sim 3\pi/4$, in an ELMing H-mode plasma overlaid with the modeling result using measured profiles and pellet parameters. (b) Same size pellet injected at 586 m/s from the outside midplane, $\chi_{c0}(0) = 0$, in an ELMing H-mode plasma overlaid with the modeling result using measured profiles and pellet parameters.

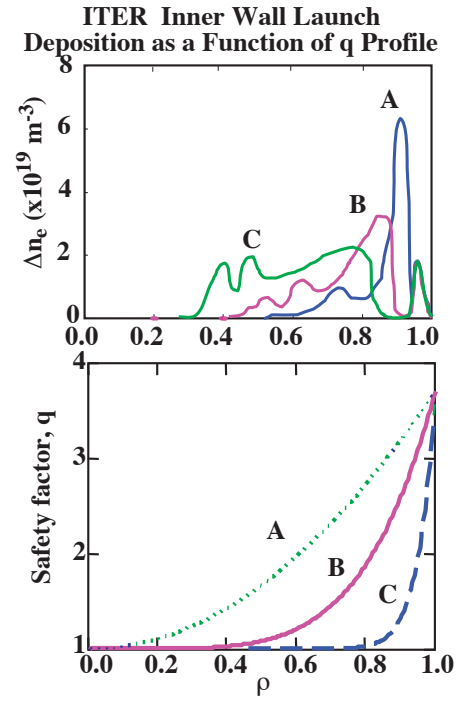

Fig. 5. (a) Fuel deposition profiles for inboard pellet injection into an ITER-like plasma with different q-profiles shown in (b).

motion is along the magnetic field lines, as expected, with speeds of about one-third of the local acoustic speed. In addition to the parallel flow there is clear evidence of some "anomalous" (numerical) transport perpendicular to the flux tube.

Figure 7 shows poloidal slices of density at the mean toroidal pellet location for inboard midplane (top frame) and outboard (bottom frame) pellet entry. At time $t = 2$ we observe the ablated mass in a cloud around the mean pellet position. At later times (t = 20, 60) the pellet ablated mass has a significant large-R displacement compared to the mean pellet location. The outboard case shows a dramatic turning around of the mass near the plasma boundary. This is due to the zero mass flux boundary condition. An outflow boundary condition would be more realistic and would likely result in a substantial loss of the ablated mass and thus poor fueling efficiency. The observed outward displacement implies that inboard pellet entry is more favorable than outboard entry, consistent with experiments.

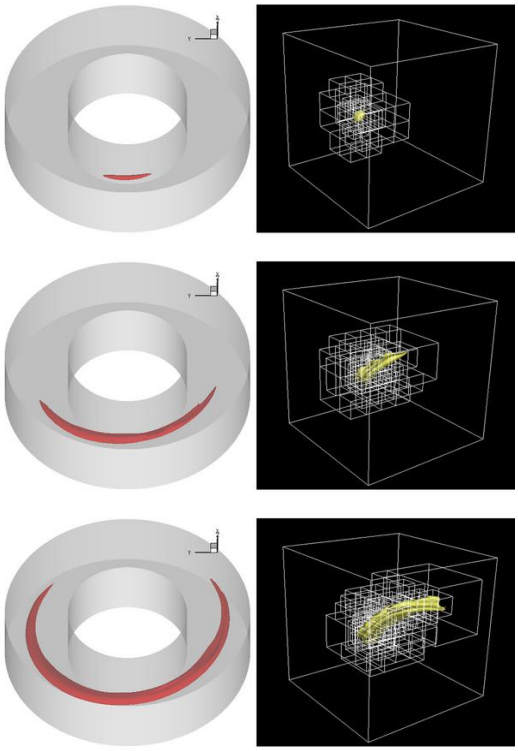

Fig. 6. (a) Snapshots of the ablated material expanding along the field lines in a tokamak at $t = 2$, 20, 60 Alfvén times. (b) Corresponding outlines of the various grids in the calculation where mesh adaptivity has taken place..

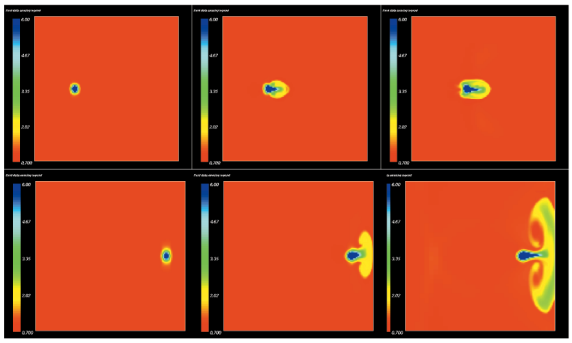

Fig. 7. Density isosurfaces in the poloidal plane of an ablating and drifting pellet cloud at three different times (5 = 0, 20, 60) for inboard (top frame) and outboard (bottom frame) pellet entry.

Acknowledgment

This research was supported in part by the U.S. Department of Energy under DE-FC02-04ER54698, DE-FG03-95ER54309, DE-AC02-76CH03073, and DE-AC05-00OR22725, and by grant-in-aid from the Ministry of Education, Culture, Sports, Science and Technology, Japan. The AMR code development also used resources of the National Energy Research Scientific Computing Center, which is supported by the Office of Science of the U.S. Department of Energy under DE-AC03-76SF00098.

References

[1] ISHIZAKI, R., PARKS, P.B., *et al.,* Phys. Plasmas **11** (2004) 4064.
[2] PARKS, P.B., and BAYLOR, L.R., submitted to Phys. Rev. Lett. (2004).
[3] ROZHANSKY, V., *et al.,* Plasma Phys. Control. Fusion **46** (2004) 575.
[4] PARKS, P.B., *et al.,* Phys. Plasmas **7** (2000) 1968.
[5] SAMTANEY, R., and JARDIN, S.C., Sherwood Fusion Theory Conf. (2004).
[6] GODUNOV, S.K., Numer. Methods Mech. Contin. Media **1** (1972) 26.
[7] COLELLA, P. J. Comput. Phys. **87** (1990) 171.
[8] CROCKETT, R., *et al..,* submitted to J. Comput. Phys. (2003).